Boosting the thermoelectric performance of math xmlns="http://www.w3.org/1998/Math/MathML">mrow>msub>mi>Fe/mi>mn>2/mn>/msub>mi>VAl/mi>mtext>−/mtext>mi>type/mi>/mrow>/math> Heusler compounds by band engineering

F. Garmroudi, A. Riss, M. Parzer, N. Reumann, H. Müller, E. Bauer, S. Khmelevskyi, R. Podloucky, T. Mori, K. Tobita, Y. Katsura, and K. Kimura

Phys. Rev. B **103**, 085202 — Published 1 February 2021

DOI: 10.1103/PhysRevB.103.085202

Boosting the thermoelectric performance of Fe_2VAl-type Heusler compounds by band engineering

F. Garmroudi* and A. Riss, M. Parzer, N. Reumann, H.Müller, E. Bauer
Institute of Solid State Physics, Technische Universität Wien, Vienna, Austria

S. Khmelevskyi
Institute of Applied Physics, Technische Universität Wien, Vienna, Austria

R. Podloucky
Institute of Physical Chemistry, Universität Wien, Vienna, Austria

T. Mori
International Center for Materials Nanoarchitectonics, National Institute for Materials Science, Tsukuba, Japan

K. Tobita, Y. Katsura, K. Kimura
Department of Advanced Materials Science, The University of Tokyo, Kashiwa, Japan

Linking the fundamental physics of band structure and scattering theory with macroscopic features such as measured temperature dependencies of electronic and thermal transport is indispensable to a thorough understanding of thermoelectric phenomena and ensures more targeted and efficient experimental research. Regarding Fe_2VAl-based compounds, experimental work has seen mostly qualitative and often speculative interpretations, preventing this class of materials from tapping their full potential when it comes to applications. In this work, the temperature-dependent Seebeck coefficient and electrical resistivity of a set of p-type and n-type samples with the composition $Fe_2V_{1-x}Ta_xAl_{1-y}Si_y$ are presented from 4 K up to 800 K as well as the Hall mobility and carrier concentration from 4 K to 520 K. We attempt a quantitative analysis of our data using a parabolic two- and three-band model and compare the model results with those from DFT calculations. Our findings show an increase of the band gap E_g from almost zero in undoped Fe_2VAl towards $E_g \approx 0.1$ eV with increasing Ta substitution, consistent with results from first-principles calculations. Due to the resulting enhancement of the Seebeck coefficient, the maximum power factor is boosted up to 10.3 mW/mK^2, which is, to the best of our knowledge, the highest value among n-type bulk semiconductor systems reported near room temperature up until now. We further show that for the p-type $Fe_2V_{1-x}Ta_xAl$ compounds, the dominant scattering mechanism of electrons is intrinsically different compared to the n-type samples, for which acoustic phonon scattering can well describe the temperature-dependent Hall mobility in a broad range of temperatures.

Keywords: DFT calculation, band gap, Seebeck coefficient, carrier mobility, power factor, Fe_2VAl

I. INTRODUCTION

Designing advanced functional materials with distinct properties is a necessity for facing future problems such as the global energy crisis. Thermoelectric materials, which can directly convert waste heat into electricity via the Seebeck effect, are especially attractive for sustainable high-end technological applications. The dimensionless figure of merit $ZT = \frac{S^2}{\rho(\lambda_e+\lambda_{latt})}T$ determines the thermoelectric conversion efficiency, with S being the Seebeck coefficient, ρ the electrical resistivity, λ_e and λ_{latt} the electronic and lattice thermal conductivity and T the absolute temperature, respectively. Among various material classes, Fe_2VAl-based full-Heusler compounds are being investigated due to a large peak of the power factor $PF = S^2/\rho$ at 300-400 K, where most waste heat is released to the environment [1–7]. Additionally, those materials consist of ubiquitous elements and have chemical and mechanical long-term stability [8, 9].

The electronic structure of stoichiometric Fe_2VAl has mostly been reported as a narrow pseudogap system, with the band gap E_g ranging from - 0.2 eV to - 0.1 eV, together with a large differential density of states (DOS) at either side of the Fermi energy E_F. This was predicted by several DFT studies [10–15] and indeed confirmed by numerous experimental works [16–18]. However, recent studies have brought into question whether an indirect narrow-band-gap semiconductor is a more accurate description of this compound [19, 20].
Nishino *et al.* found that Si doping at the Al site in Fe_2VAl can effectively optimize the charge carrier concentration through a rigid-band-like shift of E_F, which

* fabian.garmroudi@tuwien.ac.at

already allows for large values of $PF \approx 5.5\,\mathrm{mW/mK^2}$ [1]. Even higher power factors of up to $6.7\,\mathrm{mW/mK^2}$ [21] and $6.8\,\mathrm{mW/mK^2}$ [22] were found in the off-stoichiometric compounds $Fe_{2-x}V_{1+x}Al_{1-y}Si_y$ and $Fe_2V_{1+x}Al_{1-x}$ respectively. The recent focus of studies has therefore primarly been on the reduction of the large lattice thermal conductivity with encouraging results obtained by heavy elemental substitution [3, 23–25], thin film deposition [26–29] or microstructural tailoring [30]. In the case of heavy elemental substitution, Terazawa *et al.* reported on the effect of a V/Ta substitution with respect to the reduction of λ_{latt} through increased phonon scattering [23, 24]. However, the effect of this substitution with respect to the electronic structure and Seebeck coefficient is only scarcely and inconsistently reported in the literature [31, 32]. *Ab initio* calculations in the present study suggest a semimetal-insulator-like transition in the case of a full substitution of V by Ta due to its higher d-orbital energies compared to that of V (see Figure 1 and Figure 2). This should be an effective strategy for enhancing the Seebeck coefficient. In fact, a recent DFT study on Fe_2TaZ (Z=Al,Ga,In) by Khandy *et al.* predicts maximum Seebeck coefficients of almost $700\,\mu\mathrm{V/K}$ at $T = 600\,\mathrm{K}$ for optimally doped Fe_2TaAl due to the larger band gap [33]. Even for smaller doping concentrations, a partial band gap increase is noticeable in the calculated densities of states of this work. We aim to experimentally demonstrate such an opening of the band gap, causing an enhancement of the Seebeck coefficient and thermoelectric power factor. This is expected to be realised in $Fe_2V_{1-x}Ta_xAl_{1-y}Si_y$.

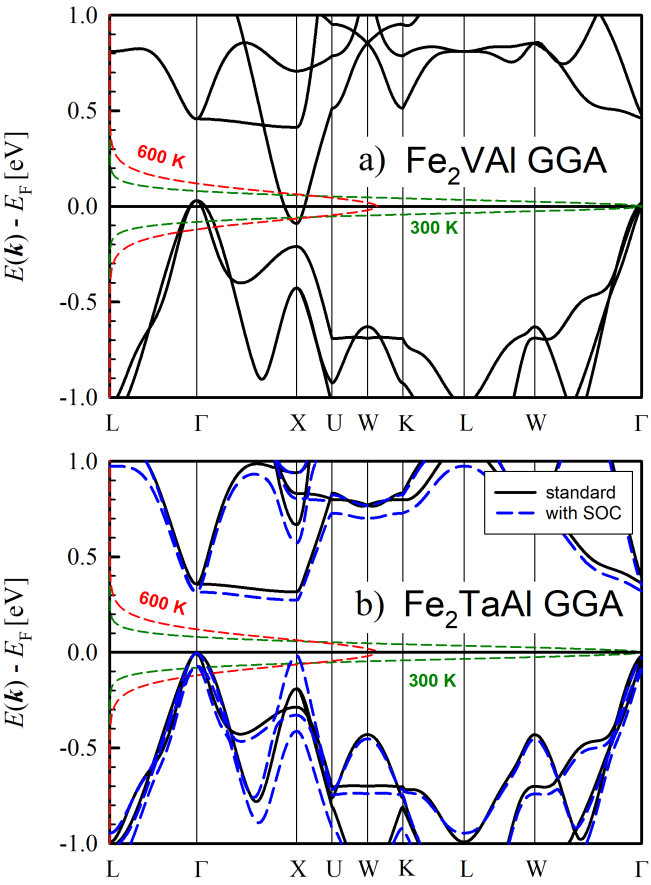

Figure 1: Calculated electronic band structures at equilibrium volume (VASP-GGA) of a) Fe_2VAl and b) Fe_2TaAl with and without spin-orbit coupling (SOC). Energy-derivative of the Fermi-Dirac distribution is plotted for $T = 300$ and $600\,\mathrm{K}$.

II. EXPERIMENTAL METHODS & COMPUTATIONAL DETAILS

Bulk elements of high purity (Fe 99.99 %, V 99.93 %, Ta 99.95 %, Al 99.999 %, Si 99.9999 %) were stoichiometrically weighed and melted by high-frequency induction heating. Polycrystalline samples of around 5 g were obtained, with a mass loss of less than 0.1 %, and evacuated in a quartz tube at $\approx 10^{-5}$ mbar for annealing at 1073 K for 168 h, followed by furnace cooling. The crystal structure was probed with Cu-Kα radiation in a Bragg-Brentano geometry. Rietveld refinements of the XRD patterns were performed and the lattice parameter was obtained. For the high temperature resistivity and Seebeck measurements a conventional four-probe dc method (ZEM3-ULVAC) was used, while for the low temperature Seebeck coefficient measurements from 4 K up to 300 K, an ac method similar to the one in Ref. [34], using a toggled heating technique ('seesaw heating'), was applied. The results for the undoped Fe_2VAl compound were taken from our previous study, where the electronic transport properties have been extensively discussed and compared with DFT-derived data using the BoltzTraP package [35]. Hall resistance was measured using the van der Pauw technique with fields up to 10 T. Alloy-averaged densities of states of samples discussed in this work were calculated using the Kohn-Korringa-Rostoker (KKR) Green function formalism under the coherent potential approximation (CPA). The experimentally obtained lattice constants were taken into account for the calculation. Futhermore, the Vienna Ab initio Simulation Package (VASP [36]) was applied for calculating the band structure and DOS of relaxated Fe_2VAl and Fe_2TaAl using the standard GGA-PBE functional for the exchange-correlation term. Regarding Fe_2TaAl, a standard non-relativistic calculation of the band structure and one taking into account spin-orbit coupling were performed. A plane-wave basis cutoff energy of 500 eV for Fe_2VAl and 600 eV for Fe_2TaAl were taken into consideration for the calculations. After structural relaxation, lattice parameters of 5.691 Å for Fe_2VAl and 5.903 Å for Fe_2TaAl were obtained, which were used for the band structure and density of states (DOS) calculations. The DOS was calculated on a grid point density of 1000/eV using the tetrahedron method with Blöchl corrections.

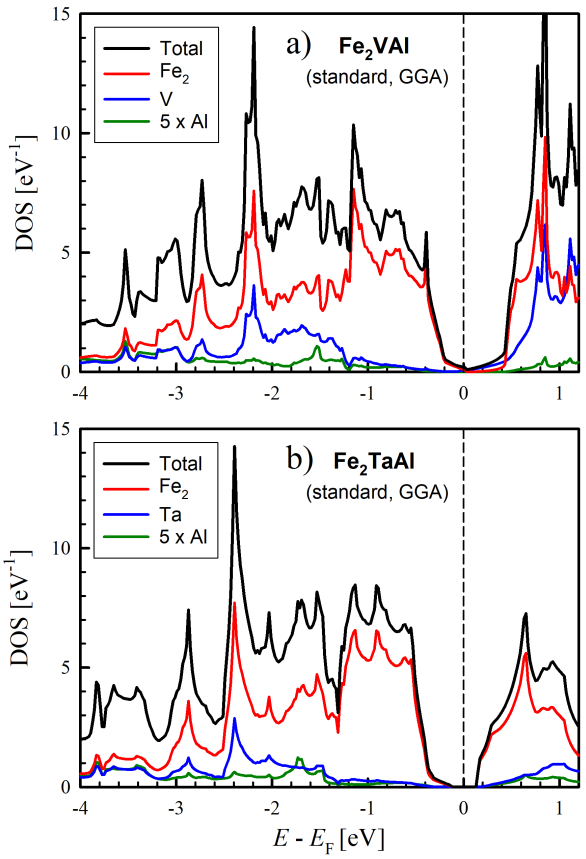

Figure 2: Energy-dependent electronic densities of states (DOS) of a) Fe_2VAl and b) Fe_2TaAl at equilibrium volume (VASP-GGA). V contributes delocalized states at the Fermi energy while the Ta conduction band states are located far above E_F.

III. RESULTS

A. Crystal structure

X_2YZ full-Heusler systems crystallize in the fully-ordered Cu_2MnAl-type crystal structure which can be interpreted as four interpenetrating *fcc* sublattices. However, anti-site disorder is a common phenomenon in Fe_2VAl-based compounds and might change the cubic crystal structure with respect to their space groups [17, 37, 38]. As can be seen in Figure 3, all samples show the typical Heusler-type ($L2_1$) structure pattern with no impurity peaks being visible. A more detailed study on the solubility limit and XRD patterns in this series of Heusler compounds can be found elsewhere [39]. The diminished intensity of the (111) Bragg peak in the diffractogram is a strong indication for a CsCl-type disorder between V and Al atoms, which share a similar surrounding in the crystal lattice. The nominal composition of the undoped sample is therefore better described as $Fe_2V_{1-x_d}Al_{x_d}Al_{1-x_d}V_{x_d}$. Rietveld refinements allow to obtain a rough approximation for the fractional disorder concentration $x_d = 0.3 \pm 0.1$. The lattice parameters in Figure 3 match previously reported values and decrease with increasing the Al/Si substitution but increase linearly with the V/Ta substitution [2, 4, 40].

B. Electronic structure

Conventional DFT-based calculations implementing a LDA or GGA-type exchange correlation potential have predominantly referenced the electronic band structure of Fe_2VAl as a semimetal with an indirect negative band gap, meaning an overlap of bands at different high symmetry points in k-space. As illustrated in Figure 1a, a threefold degenerate hole pocket lies near E_F at the Γ point and a sixfold degenerate electron half pocket is located at the X point of the first Brillouin zone. Those bands show a highly dispersive character. While the valence band is dominated by Fe states, the conduction band is controlled by V states. GGA calculations using VASP were also conducted for a complete substitution

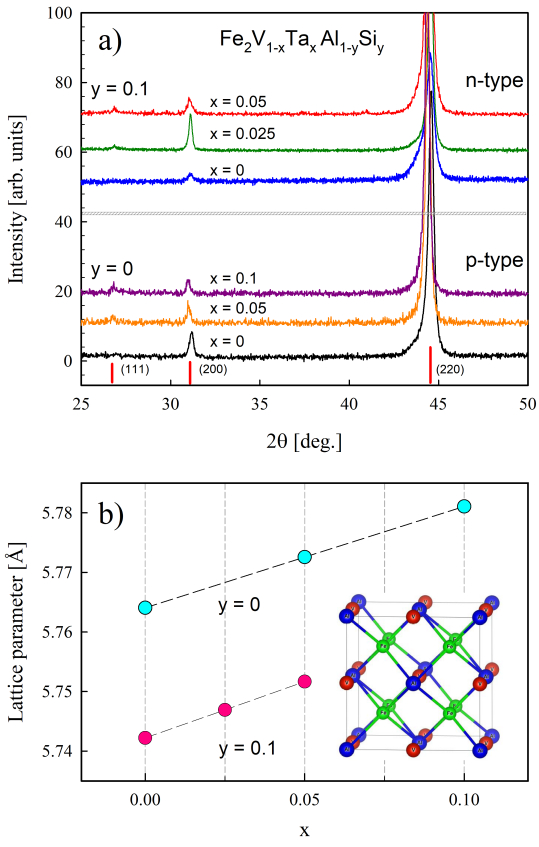

Figure 3: XRD powder patterns of $Fe_2V_{1-x}Ta_xAl_{1-y}Si_y$ (upper panel) and concentration-dependent lattice parameters taken at room temperature (lower panel). The inset sketches the crystal structure of Fe_2VAl.

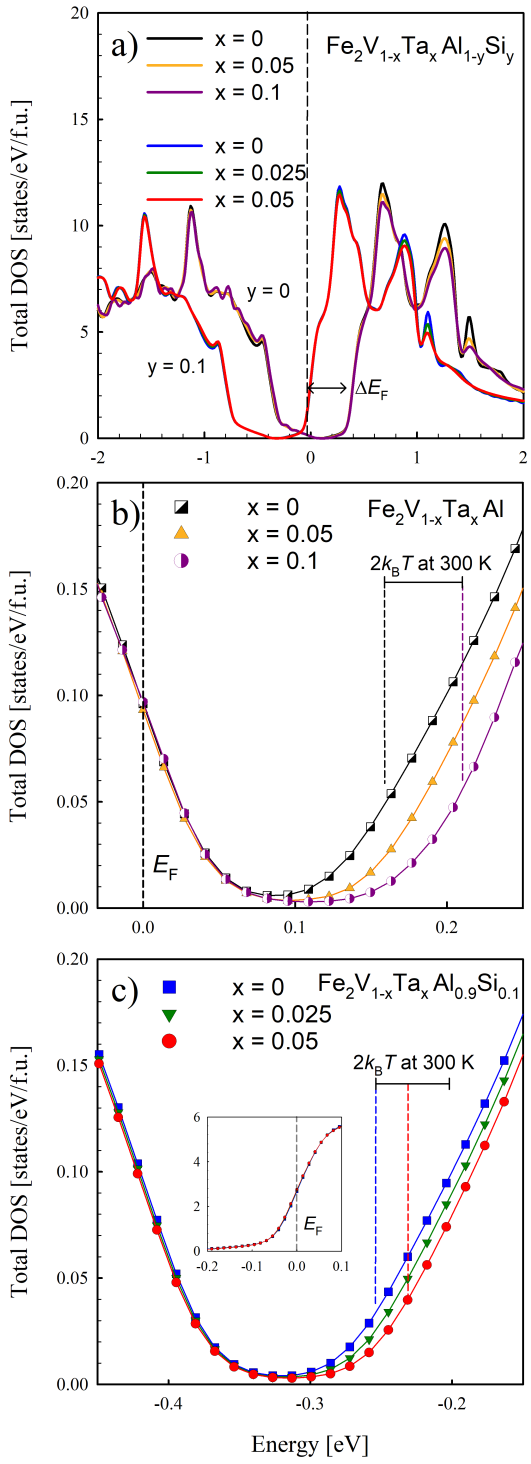

Figure 4: Energy-dependent DOS (KKR-CPA) of $Fe_2V_{1-x}Ta_xAl_{1-y}Si_y$ at the respective experimental volume. The first panel (a) demonstrates a rigid-band-like shift of the Fermi energy caused by the Al/Si substitution, while the panels b) and c) show an opening of the pseudo band gap towards the conduction band side, which is caused by the V/Ta substitution.

of Ta on the V site of the $L2_1$ Heusler structure. The electronic band structure and DOS are shown in Figure 1b and Figure 2b, respectively. A complete opening of the band gap can be observed, as the dispersive Ta states are located well above the Fermi energy. Taking into account spin-orbit coupling for Fe_2TaAl reveals slight modifications in the electronic band structure with the most notable being a convergence of the Γ and X valence bands. The energy-derivative of the Fermi-Dirac distribution, added in Figure 1, shows that the energy range which heavily contributes to electronic transport is confined around the highly dispersive Γ valence bands and the X conduction band in Fe_2VAl. Decreasing the bipolar conduction by opening the pseudogap should thus have a very promising effect on the Seebeck coefficient. In order to understand the partial substitution effect on the electronic structure, alloy-averaged densities of states were calculated for all $Fe_2V_{1-x}Ta_xAl_{1-y}Si_y$-type samples synthesized and measured in this work. The Kohn-Korringa-Rostoker coherent potential approximation method (KKR-CPA) was applied, taking into account the experimentally derived room temperature lattice parameters. Figure 4a shows the rigid-band-like shift of E_F from the valence band edge towards the steep slope of the conduction band caused by the Al/Si substitution. Figure 4b shows a magnified image of the band gap, where the DOS is governed by the previously mentioned dispersive bands. It should be noted that for $Fe_2V_{1-x}Ta_xAl$ the Fermi energy is located at the tail of the Γ valence bands but much farther in the conduction band for $Fe_2V_{1-x}Ta_xAl_{1-y}Si_y$, where the total DOS has a steep slope and is about two orders of magnitude larger.

C. Electronic transport

Seebeck coefficient

Figure 5a and Figure 5b show the temperature-dependent Seebeck coefficient S from 4 K up to 800 K for various concentrations x of $Fe_2V_{1-x}Ta_xAl$ (p-type samples) and of $Fe_2V_{1-x}Ta_xAl_{0.9}Si_{0.1}$ (n-type samples), respectively. The sign of S changes upon substituting Si on the Al site due to the rigid-band-like shift of E_F into the conduction band (see Figure 4a) resulting in a change of predominant charge carrier type from holes to electrons. It can be further seen that the maximum values of the Seebeck coefficient S_{max} in Figure 4a increase with Ta concentration as a consequence of the band gap increase. Moreover, the low temperature slope of $S(T)$, which corresponds inversely to the carrier concentration in the single band picture, remains almost the same for all p-type samples, but gradually increases with x in the n-type samples. This is in accordance with the opening of the band gap as demonstrated in Figure 4b and Figure 4c. The experimental data are analyzed within a parabolic two-band (2PB) and three-band (3PB) model

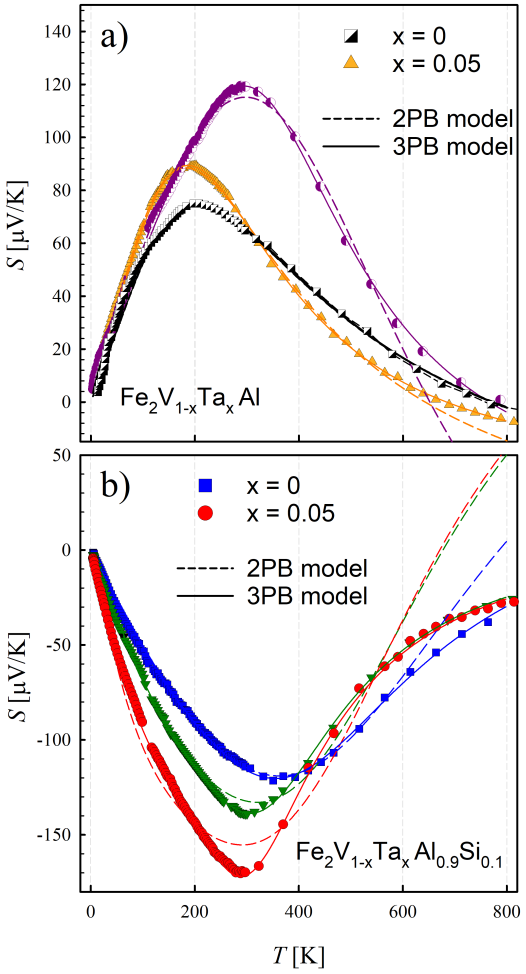

Figure 5: Temperature-dependent Seebeck coefficient of a) $Fe_2V_{1-x}Ta_xAl$ and b) $Fe_2V_{1-x}Ta_xAl_{0.9}Si_{0.1}$ for various concentrations of x. Dashed and solid lines represent least squares fits calculated within a parabolic two-band (2PB) and three-band (3PB) model, respectively. Details are explained in the text.

(dashed and solid lines), which will be reviewed in detail in section V.

Electrical resistivty

Figure 6 summarizes the electrical resistivity of all samples discussed in this work. A drastic change upon Al/Si substitution towards a more metallic-like nature at low temperatures is observed, which is overlain by a semiconducting contribution at higher temperatures. This is in accordance with previous observations on $Fe_2VAl_{1-y}Si_y$ [1, 4]. As the isoelectronic substitution of V/Ta does not add any excess valence electrons, a semiconductor-like behavior of Fe_2VAl that has been reported in the literature [5, 41] remains for the p-type

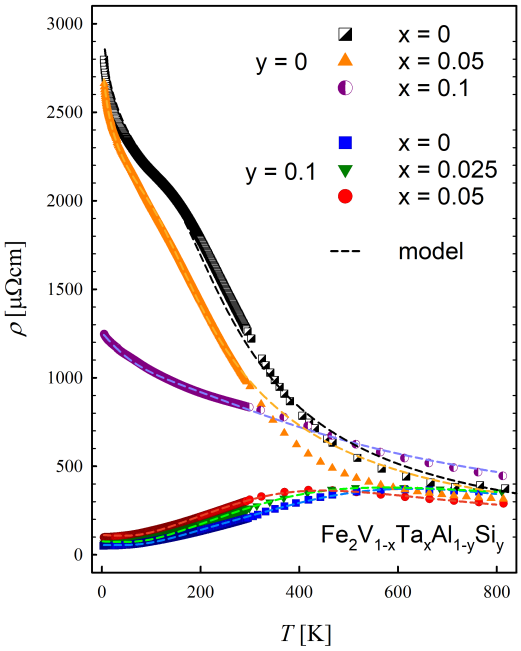

Figure 6: Temperature-dependent electrical resistivity of $Fe_2V_{1-x}Ta_xAl_{1-y}Si_y$. Dashed lines represent least squares fits as explained in the text.

samples. It can be seen that the residual resistivity ρ_{4K} strongly decreases in $Fe_2V_{1-x}Ta_xAl$ as x goes from 0 towards 0.1, whereas ρ_{4K} even slightly increases with Ta doping in the n-type samples $Fe_2V_{1-x}Ta_xAl_{0.9}Si_{0.1}$. In order to investigate this peculiar effect, measurements of the Hall carrier concentration and mobility were performed from 4 K up to 520 K. Such study can help to microscopically understand the resistivity behavior and is still lacking in the literature for this class of materials.

Hall mobility & carrier concentration

The Hall mobility μ_H and carrier concentration n_H were evaluated from measurements of the Hall resistivity ρ_{xy} in the linear response regime (low magnetic field limit). The magnetic field dependence of the Hall resistivity of $Fe_2V_{0.95}Ta_{0.05}Al$ and $Fe_2V_{0.95}Ta_{0.05}Al_{0.9}Si_{0.1}$ is shown in the Supplemental Materials. With some exceptions, a linear magnetic field dependence was observed for all temperatures. While for $Fe_2V_{1-x}Ta_xAl$ ρ_{xy} is always positive, which implies hole dominant transport, Si-doped samples show a negative Hall effect, corresponding to electron dominant transport. This is consistent with our measurements of the Seebeck coefficient. Despite the linear Hall effect, bipolar transport should be expected in these compounds, as suggested by the temperature-dependent behavior of both the Seebeck coefficient and electrical resistivity. Therefore, the mobilities and carrier concentrations shown in this work merely represent the

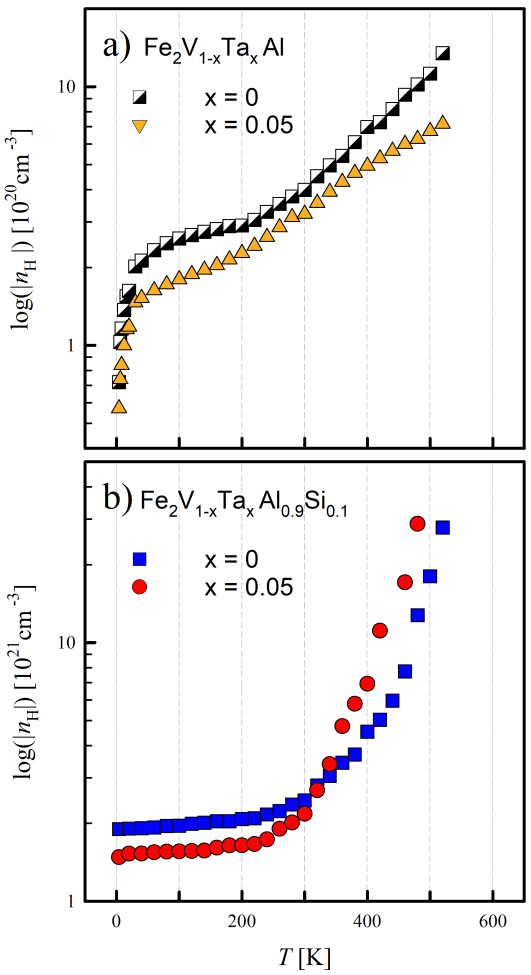

Figure 7: Temperature-dependent charge carrier concentration of a) $Fe_2V_{1-x}Ta_xAl$ and b) $Fe_2V_{1-x}Ta_xAl_{0.9}Si_{0.1}$.

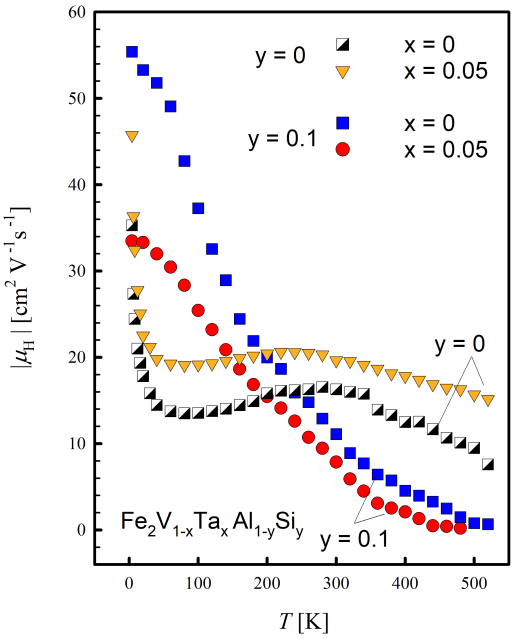

Figure 8: Temperature-dependent Hall mobility of $Fe_2V_{1-x}Ta_xAl_{1-y}Si_y$.

interplay of electron and hole contributions, much like the Seebeck coefficient.

Inspecting Figure 7 and Figure 8, it can be seen that both $n_H(T)$ and $\mu_H(T)$ display very different temperature-dependent behaviors for the p-type and n-type samples. While $n_H(T)$ is almost constant up to 300 K in Si-doped samples, typical for metals, a steep increase of the carrier concentration at low temperatures is found for $Fe_2V_{1-x}Ta_xAl$. The absolute values of the carrier concentration are about one order of magnitude higher in the n-type samples, causing the drastic decrease of ρ mentioned above.

The Hall mobilities shown in Figure 8 demonstrate distinct differences between p-type and n-type samples. While for the latter a monotonic decrease with increasing temperatures is observed over the whole temperature range, $\mu_H(T)$ becomes almost constant for the former and even increases from 100 to 300 K. In addition, $\mu_H(T)$ increases with Ta doping for the p-type samples, but is reduced for the n-type samples. We aim to rationalize this utterly different behavior in section V, using the 2PB parameters, as derived from the Seebeck coefficient modeling, to account for multiband contributions.

In conclusion, the temperature-dependent electrical resistivity of the n-type samples is mostly dictated by $\mu(T)$ up to 300 K resulting in a metallic-like behavior, due to the almost constant charge carrier density $n_H(T)$. The distinct increase of the carrier concentration above room temperature explains the semiconductor-like contribution to $\rho(T)$ in Si-doped samples at higher temperatures. Contrarily, $Fe_2V_{1-x}Ta_xAl$ shows a weak temperature dependence of the mobility above 100 K, indicating that electron scattering might be fundamentally different in these compounds compared to the former.

IV. MODELING OF ELECTRONIC TRANSPORT

The measured experimental data in section III will be analyzed by means of different phenomenological multicarrier transport models. Since the temperature-dependent Seebeck coefficient is more sensitive towards the electronic band structure than the electrical resistivity or mobility, which also heavily depend on the carrier scattering, we started our analysis by least squares fitting $S(T)$ in a wide temperature range.

The total Seebeck coefficient with contributions from an arbitrary number of bands can be expressed by its respective single-band contributions S_i, which have to be weighted by the respective single-band electrical conduc-

tivities σ_i

$$S_{\mathrm{tot}} = \frac{\sum_i N_{v,i} S_i \sigma_i}{\sum_i N_{v,i} \sigma_i}, \tag{1}$$

where $N_{v,i}$ are the band degeneracies and i is the parabolic band index. In the case of two bands, and by making the substitution $\sigma_i^* := m_i \sigma_i$, the total Seebeck coefficient can be written as

$$S_{\mathrm{tot}} = \frac{S_1\,\sigma_1^* + \varepsilon\; S_2\,\sigma_2^*}{\sigma_1^* + \varepsilon\,\sigma_2^*}, \tag{2}$$

where we defined ε as

$$\varepsilon := \frac{N_{v,2}}{N_{v,1}} \frac{m_1}{m_2}. \tag{3}$$

In this notation, both $S_{1,2}$ and $\sigma_{1,2}^*$ only depend on the reduced chemical potential $\eta_i = E_{\mathrm{F},i} - E_{\mathrm{g},i}$ ($i = 1, 2$). Furthermore, it can be quickly seen that the total temperature-dependent Seebeck coefficient does neither depend on the absolute values of the degeneracies nor the effective masses, but only on their mutual relationship ε. The distance of the Fermi level towards the first band ΔE_{F}, the band gap E_{g} as well as ε were set as the fitting parameters of our model. We presumed $m_1 = m_e$ and $N_{v,1} = N_{v,2}$. These *ad hoc* assumptions will not influence the fitted band gap and Fermi level, but only the conduction band mass m_2, which can be quickly recalculated through ε, when different *ad hoc* parameters are guessed. All of the fitting parameters have a unique effect on $S(T)$. Thus, when modeling $S(T)$ in a wide temperature range, unambiguous results are assured. After using our experimental Seebeck data in this spectroscopic way, we proceeded by attempting to model the electrical resistivity and Hall mobility, taking into account the very same band parameters to test the validity of the model and extract further microscopic information regarding carrier scattering mechanisms. The total Hall mobility for carrier transport with multiband contributions can be modeled by weighting the single-band mobilities μ_i with the respective carrier densities n_i and charges q_i ($q = \pm e$ for holes and electrons, respectively)

$$\mu_{\mathrm{H,tot}} = \frac{\sum_i N_{v,i}\, q_i\, |n_i|\, \mu_i^2}{\sum_i N_{v,i}\, q_i\, |n_i|\, \mu_i}. \tag{4}$$

The single-band mobilities μ_i are negative for electrons and positive for holes like the Seebeck coefficient, following the usual notation. The following section will discuss the model results and aim to rationalize the experimental data, presented in the previous section.

V. DISCUSSION

Seebeck coefficient and band gap

The Seebeck coefficient heavily depends on the energy dependence of the charge carrier mobility $\mu(E)$ and the carrier density $n(E) = N(E)f(E)$, where $N(E)$ is the electronic density of states (DOS) and $f(E)$ is the Fermi-Dirac distribution. As an approximation this relationship between S, μ and n can be expressed by the well-known Mott formula [42]

$$S = \frac{\pi^2}{3} \frac{k_{\mathrm{B}}^2}{-e} T \left(\frac{1}{n(E)} \frac{\partial n(E)}{\partial E} + \frac{1}{\mu(E)} \frac{\partial \mu(E)}{\partial E} \right) \Bigg|_{E_{\mathrm{F}}}. \tag{5}$$

Band structure calculations predict that the substitution of V by Ta leads to slight modifications of the DOS above E_{F}, resulting in an opening of the pseudogap towards the conduction band side (see Figure 4). In order to substantiate this claim, we employed the parabolic band (PB) model, whose applicability for this class of materials was demonstrated in a recent study by Anand *et al.* [19]. While the analyses in terms of the 2PB and 3PB model (see the Supplemental Materials Sec. 3) of the temperature-dependent Seebeck coefficient of Fe_2VAl reveal a small band gap of $E_{\mathrm{g}} = \text{-}\,0.03 - 0.002\,\mathrm{eV}$, E_{g} increases up to $0.08 - 0.1\,\mathrm{eV}$ in $Fe_2V_{0.9}Ta_{0.1}Al$. In the following we will demonstrate that the enhancement of S due to the V/Ta substitution is best described by this increase of the band gap. Therefore, by simulating the band structure with parabolic bands, a relation between the temperature-dependent behavior of S and E_{g} is established.

At low temperatures, where $S(T)$ remains almost linear and is mostly governed by the influence of a single parabolic band, one can write

$$|S| = \frac{\pi^2 k_{\mathrm{B}}^2}{2e} \frac{T}{E_{\mathrm{F}}^{\mathrm{sb}}}. \tag{6}$$

Equation 6 infers that the slope $\partial S/\partial T$ is inversely proportional to the effective single-band Fermi level $E_{\mathrm{F}}^{\mathrm{sb}}$, where $E_{\mathrm{F}}^{\mathrm{sb}}$ denotes the distance from the conduction band bottom $E_{\mathrm{min}}^{\mathrm{c}}$ or from the valence band top $E_{\mathrm{max}}^{\mathrm{v}}$ to the Fermi energy E_{F} (compare Figs. 9a,b). Figure 5a shows the maximum of $S(T)$ of $Fe_2V_{1-x}Ta_xAl$ is shifted towards lower temperatures, as x increases from 0 towards 0.05, corresponding to a reduction of $E_{\mathrm{F}}^{\mathrm{sb}}$. This effect can easily be understood when looking at the calculated band structures of Fe_2VAl and Fe_2TaAl in Figure 1; it is also illustrated in the left panel of Figure 9a. The d-states of the dispersive Ta conduction band are located well above E_{F}. Therefore, the V/Ta substitution causes electrons to occupy free states in the dispersive Fe valence band, temporarily raising E_{F} and lowering $E_{\mathrm{F}}^{\mathrm{sb}}$. This causes a shift of S_{max} towards lower temperatures as the Ta content x goes from 0 towards 0.05. However, the slope $\partial S/\partial T$

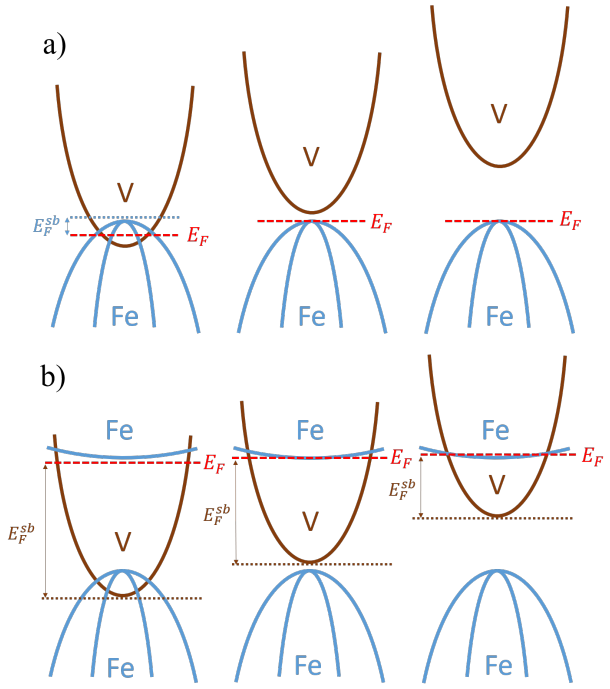

Figure 9: Schematic sketch of the V/Ta substitution effect on the electronic band structure and band gap of Fe_2VAl-based a) p-type and b) n-type samples. The energy scaling is in arbitrary units.

remains almost equal up to $S_{\max}$ for $Fe_2V_{1-x}Ta_xAl$ as x goes from 0.05 towards 0.1. This is another strong indication for the postulated band gap increase, where the conduction band bottom surpasses E_F (sketched in the middle and right panel of Figure 9a). With the Fermi level below the conduction band edge, an increase of E_g will no longer cause a significant variation of E_F^{sb}, thus yielding a similar slope of $S(T)$.

For $Fe_2V_{1-x}Ta_xAl_{0.9}Si_{0.1}$ (n-type samples) shown in Figure 5b, the temperature-dependent Seebeck coefficient is more complicated and will be discussed in the following. Opposed to the p-type samples, the Fermi level is now located close to a flat non-parabolic Fe band (Figure 9b), characterized by a steep incline in the electronic DOS (Figure 4a). Least squares fits in terms of the 2PB model yield band gaps $E_g = 0.12, 0.14, 0.16\,eV$ for $x = 0, 0.025, 0.05$, respectively, contradicting the sometimes claimed rigid-band-like shift of E_F in this series of compounds [1, 4]. Even though the absolute value of E_g may differ from the proper value for the n-type samples, the tendency of the band gap increase with Ta substitution is still apparent. Furthermore, the maxima of $S(T)$, $(T^S_{\max}, S_{\max})$ shift towards lower temperatures, in contrary to what one would intuitively expect for an increasing band gap. The explanation to that effect requires a combination of two distinct phenomena (see Figure 9b):

i) E_F is almost fixed in its position.
ii) E_g increases between the two parabolic bands.

While ii) is effectively caused by the Ta substitution as previously established, i) is caused by the presence of the strongly localized flat Fe band that provides an abundance of free states for the electrons, which have been removed from below E_F. Accordingly, the shift of E_F is significantly slowed down by this barrier and E_F^{sb} decreases. This explains the continuously increased slope of $S(T)$ with increasing the Ta content as observed in Figure 5b.

Employing the PB model, the temperature-dependent Seebeck coefficient is sketched in Figure 10, highlighting the dependence of $S_{\max}$ and $T^S_{\max}$ if the band gap E_g is varied ($0.04 \leq E_g \leq 0.13\,eV$). Here, the model calculations assume a fixed position of E_F inside the valence and conduction band for p- and n-type samples, respectively. To summarize, the values of $S_{\max}$ are shifted towards higher temperatures in case of p-type and lower temperatures for n-type samples; curves calculated in terms of the PB model reveal convincing agreement with the experimental data.

Values of the band gap have also been approximated using the Goldschmid-Sharp formula [43]

$$E_g^{GS} = 2e|S_{\max}|T^S_{\max}, \tag{7}$$

and are compared to the values obtained by the PB model in Table I.

Figure 11 shows the Seebeck coefficient at $T = 300\,K$ versus the chemical carrier concentration for the majority of substitution studies from literature [1–5, 7, 23, 25, 44–49], together with data derived in the present study. The

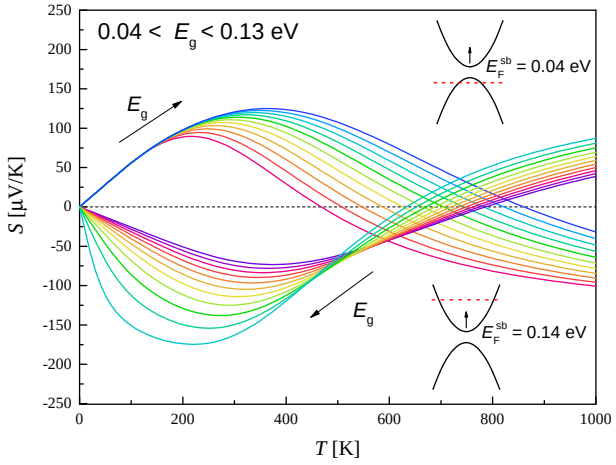

Figure 10: Temperature and band gap dependence of the Seebeck coefficient for a fixed position of the Fermi energy E_F inside the valence and conduction band; calculated within a parabolic two-band model.

Table I: Band gaps and maximum Seebeck coefficients of $Fe_2V_{1-x}Ta_xAl_{1-y}Si_y$.

	x	E_g^{GS} [eV]	E_g^{2PB} [eV]	S [μV/K]
$y = 0$	0	0.02	0.002	75
	0.05	0.04	0.02	90
	0.1	0.07	0.1	120
$y = 0.1$	0	0.08	0.12	- 120
	0.025	0.09	0.14	- 140
	0.05	0.1	0.16	- 170

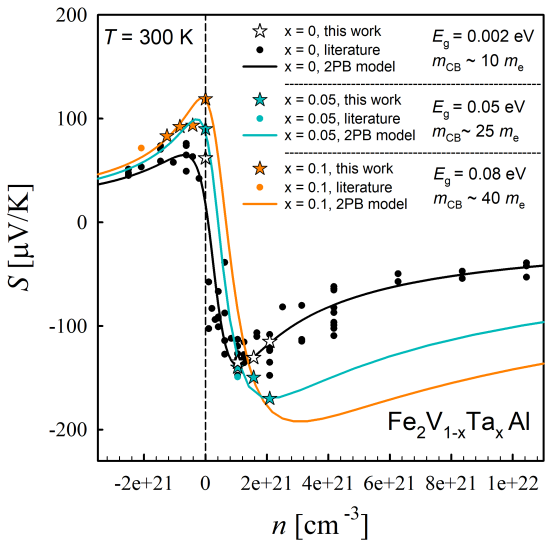

Figure 11: Seebeck coefficient versus carrier concentration for different concentrations of Ta in $Fe_2V_{1-x}Ta_xAl$, compared with data from literature. The solid lines are calculated within a parabolic two-band model for varying band gaps and effective masses.

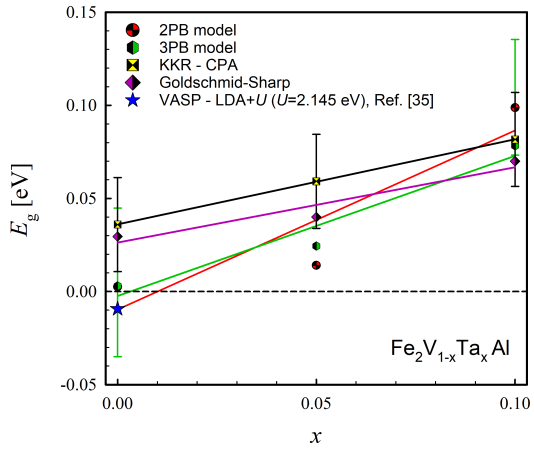

Figure 12: Concentration-dependent increase of the band gap of $Fe_2V_{1-x}Ta_xAl$ obtained from various phenomenological models and DFT calculations.

opening of the band gap as shown in this work leads to the largest obtained p-type and n-type values of the Seebeck coefficient for stoichiometric Fe_2VAl-based samples so far. Besides the band gap modifications, an increase of the effective mass is likely in $Fe_2V_{1-x}Ta_xAl$ and in $Fe_2V_{1-x}Ta_xAl_{0.9}Si_{0.1}$ due to the band convergence in the conduction band, resulting in a shift of S_{max} towards higher carrier concentrations.

Figure 12 summarises the opening of the band gap with increasing Ta content in $Fe_2V_{1-x}Ta_xAl$, consistently predicted by various phenomenological models and *ab initio* calculations. The band gap extracted from the VASP calculations is in good agreement with the parabolic band model if the standard GGA functional is replaced by an LDA+U approach ($U = 2.145$ eV) in the calculations [35].

In conclusion, the effect of the V/Ta substitution on thermoelectric transport is best described by band convergence in the conduction band and an increase of the band gap, which has a unique impact on the temperature-dependent Seebeck coefficient. The various features observed are well accounted for within a PB model. This model also yields good quantitative agreement with *ab initio* calculations based on the KKR-CPA method as well as the VASP code if an enhanced exchange correlation (LDA+U with $U = 2.145\,eV$ [35]) is considered.

Electrical resistivity

In general, the electrical resistivity within the parabolic band model is related to band-specific and band-independent parameters and can be written as

$$\rho(T) = \frac{1}{\sum_i \sigma_i(T)} = \frac{1}{KT^{\beta+3/2}\sum_i \frac{1}{m_i^*} F_0(\eta_i, T)}, \quad (8)$$

where K is a constant prefactor and β is a coefficient for the temperature-dependent mobility, independent of the band structure. In the case of acoustic phonon scattering $\beta = -\frac{3}{2}$, whereas $\beta = -\frac{1}{2}$ for alloy-disorder scattering. $F_0(\eta_i, T)$ is the Fermi integral of 0^{th} order for each band depending on the reduced chemical potential. Both have been obtained from above-mentioned Seebeck coefficient modeling and are characteristic band parameters. Varying only the band-independent parameters K and β in Equation 8, the fits obtained in Figure 13 show a fairly

Table II: Parameters derived from modeling the electrical resistivity of $Fe_2V_{1-x}Ta_xAl_{1-y}Si_y$. The absolute values for the fitting parameters shown in brackets are questionable, as explained in the text.

	x	β	Θ_D [K]	v_s [m/s]
$y = 0$	0	- 0.5	(803)	(6250)
	0.05	- 0.4	(700)	(5510)
	0.1	- 0.3	(598)	(4760)
$y = 0.1$	0	- 1.8	704	5540
	0.025	- 1.7	637	5015
	0.05	- 1.6	514	4050

good agreement with the measured high temperature resistivity. This corroborates the previously drawn picture of band structure modifications rendered in Figure 9.

The experimentally obtained low temperature resistivity data, however, can hardly be understood within this model, since a more detailed consideration of the electron-phonon interaction is necessary. As succesfully applied in several previous studies [25, 50], the Bloch-Grüneisen formula can be combined with a temperature-dependent carrier density for modeling $\rho(T)$ of such materials. Results of least squares fits are shown as dashed lines in Figure 6, revealing a reasonable estimation of parameters such as the Debye temperature Θ_D. The latter can be used to calculate the mean sound velocity v_s. The values obtained for β, Θ_D and v_s are summarised in Table II. Considering the values of β as well as the temperature-dependent behavior of the Hall mobility, we suggest that the carrier scattering mechanism in the p-type compounds is inherently different than for the n-type samples and cannot be understood by simple electron-phonon scattering. Thus, absolute values for the Debye temperatures and sound velocities are questionable and shown in brackets. For the n-type samples, where a considerable contribution of acoustic phonon scattering can be expected, more meaningful results are obtained. However, the Debye temperatures are still slightly overestimated compared to the directly measured values from literature [51, 52], which showcases the limits of the phenomenological models in the presence of anti-site defects and disorder, which notably influence carrier transport even in the extrinsic n-type samples.

The sound velocities and Debye temperatures decrease and the lattice becomes less stiff with Ta doping. The tendency of a softening of the crystal lattice is further substantiated from an evolution of the deformation potential. Considering again the parabolic band model, it can be seen that the fit parameter β is closer

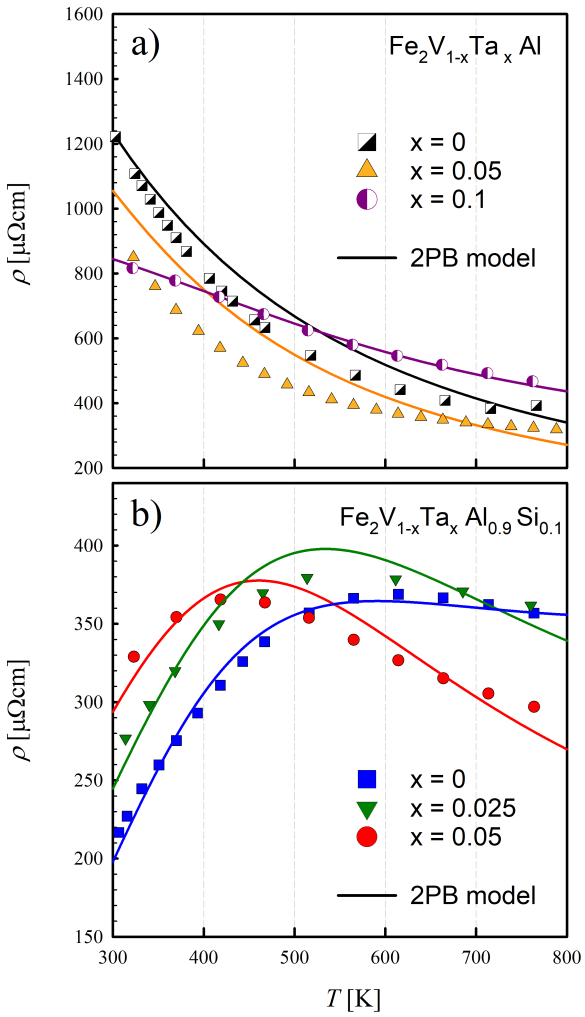

Figure 13: Temperature-dependent electrical resistivity above 300 K for a) $Fe_2V_{1-x}Ta_xAl$ and b) $Fe_2V_{1-x}Ta_xAl_{0.9}Si_{0.1}$ modeled with parabolic band parameters obtained from fitting the temperature-dependent Seebeck coefficient.

to the alloy-disorder scattering limit in $Fe_2V_{1-x}Ta_xAl$ (p-type), while it is closer to acoustic phonon scattering in $Fe_2V_{1-x}Ta_xAl_{0.9}Si_{0.1}$ (n-type). Even in undoped Fe_2VAl disorder scattering seems to play an important role, which might be due to intrinsic anti-site defects, as suggested by the low X-ray intensity of the (111) Bragg peak in Figure 3 and also a large negative magnetoresistance at low temperatures (Supplemental Information).

Mobility and scattering potentials

The impact of the charge carrier interaction with long-wave-length acoustic phonons is proportional to the deformation potential Ξ_{ph}, which, in first approximation, describes the electronic band structure modifications due

to collective lattice vibrations. Here, we treated Ξ_{ph} as a band-independent fitting parameter that relates to the single-band mobility for acoustic phonon scattering [53]

$$\mu_{\mathrm{ph},i} = \frac{\sqrt{2}\pi e\hbar^4}{3(k_{\mathrm{B}}T)^{3/2}} \frac{v_{\mathrm{l}}^2 d_{\mathrm{m}}}{\Xi_{\mathrm{ph}}^2} \frac{F_0(\eta_i)}{F_{1/2}(\eta_i) m_i^{*5/2}}, \tag{9}$$

where d_{m} is the material density and v_{l} is the longitudinal sound velocity, which was reasonably approximated to the mean sound velocity v_{s} by $v_{\mathrm{l}} = 1.53\, v_{\mathrm{s}}$. On the other hand, the alloy-disorder scattering constant U_{d} denotes the local potential perturbations caused by atomic disorder and neutral impurities. It relates to the mobility μ_{dis} via the Brooks formula [54]

$$\mu_{\mathrm{dis},i} = \frac{16e\hbar^4}{9\sqrt{2}(k_{\mathrm{B}}T)^{1/2}} \frac{N_0}{(x_{\mathrm{d}} - x_{\mathrm{d}}^2) U_{\mathrm{d}}^2} \frac{F_0(\eta_i)}{F_{1/2}(\eta_i) m_i^{*5/2}}, \tag{10}$$

with N_0 being the number of atoms per unit volume. For the p-type samples, we considered another scattering mechanism with ionized impurity scattering, where the mobility increases with temperature

$$\mu_{\mathrm{ion},i} \propto T^{3/2} \frac{F_0(\eta_i)}{F_{1/2}(\eta_i)}. \tag{11}$$

The Mathiessen rule can be used for multiple scattering mechanisms by summing up the reciprocal values of independent scattering times. Thus, the temperature-dependent mobility for combined scattering mechanisms is given by

$$\mu_{\mathrm{comb},i}(T) = \frac{\mu_{\mathrm{ph},i}(T)\, \mu_{\mathrm{dis},i}(T)\, \mu_{\mathrm{ion},i}(T)}{\mu_{\mathrm{ph},i}(T) + \mu_{\mathrm{dis},i}(T) + \mu_{\mathrm{ion},i}(T)}. \tag{12}$$

For the total mobility from two or more bands, the mobility has to be weighted with the respective carrier densities n_i as described in section IV. This allows to model the temperature-dependent Hall mobility and extract information about the dominant scattering mechanisms that limit carrier transport.

In Figure 14a the temperature-dependent mobility is modeled using Equations 9 and 10. For Fe_2VAl, both acoustic phonon and disorder scattering can describe the data reasonably well only above room temperature. As the Ta concentration in $Fe_2V_{1-x}Ta_xAl$ is increased from 0 to 0.05, only disorder scattering traces the temperature-dependent mobility fairly well, while pure phonon scattering misses the respective temperature dependence. Below room temperature, both of these interactions fail to account for the experimentally obtained mobility data. This suggests that the scattering mechanism in these samples might be fundamentally different and further interaction processes need to be taken into consideration. A recent investigation of the charge transfer in undoped Fe_2VAl, derived by Bader's approach, suggests that all three atoms in the ternary compound become ionized, as a significant charge transfer from Al and V to the neighbouring Fe atoms occurs [35]. Hence, additionally taking inonized impurity scattering into account, Equation 11 indeed allows for a much better fitting in the whole temperature range above 100 K (solid lines Figure 14a). Therefore, we presume that ionized and/or magnetic anti-site defects might be the cause for the total failure of Equations 9 and 10 to describe the experimental mobility data below 300 K. As the exact influence of anti-site disorder and phonon scattering is unclear in the present p-type samples, a quantitative description about the scattering potentials U_{d}, Ξ_{ph} and their evolution with V/Ta substitution is hardly feasible. Despite the softening of the lattice as well as the induced atomic disorder by heavy Ta atoms, the electron mobility consistently increases in $Fe_2V_{1-x}Ta_xAl$ for $x = 0 \rightarrow 0.05$ and even for the sample with $x = 0.1$, which is not shown here.

The n-type samples $Fe_2V_{1-x}Ta_xAl_{0.9}Si_{0.1}$, on the other hand, exhibit an opposite behavior and the Ta-doped sample shows lower values of μ_{H} in the whole temperature range. We suppose that the band convergence and increase of effective mass, mentioned in Figure 9 are most likely responsible for this effect, together with the increased atomic disorder upon alloying.

Figure 14b reveals a monotonic decrease of μ_{H} with temperature for both n-type samples. Most convincing least squares fits are revealed, assuming only phonon scattering to be the limiting scattering mechanism for the mobility. This allows to evaluate the phonon deformation potential. Using a valence band mass of $a \cdot m_e$ ($a \in \mathbb{R}$), the deformation potential decreases from $\Xi_{\mathrm{ph}} = 3.6 \cdot |a|^{5/2}$ to $1.9 \cdot |a|^{5/2}$ eV upon increasing the Ta concentration from $x = 0$ up to 0.05. This is a substantial reduction of the elctron-phonon interaction by more than 47%. The decrease in Ξ_{ph} almost compensates the decrease of the sound velocities and the disorder from alloying as well as the increasing conduction band mass, yielding comparable values of μ_{H} for the n-type samples above room temperature. In a recent work on $Fe_2V_{1-x}W_xAl$ bulk systems, we showed that the experimentally obtained electron mobility increases signficantly as x goes from 0.05 up to 0.2, against all common expectations that the mobility should decrease due to the decreased sound velocities and substantial disorder caused by the V/W substitution [25]. Consistent with our current interpretation, this might also be attributed to a reduction of the phonon deformation potentials. If similar tendencies can be likewise observed for other 5d heavy elements, this might pave the way for a new strategy of increasing the thermoelectric performance in Fe_2VAl-based compounds.

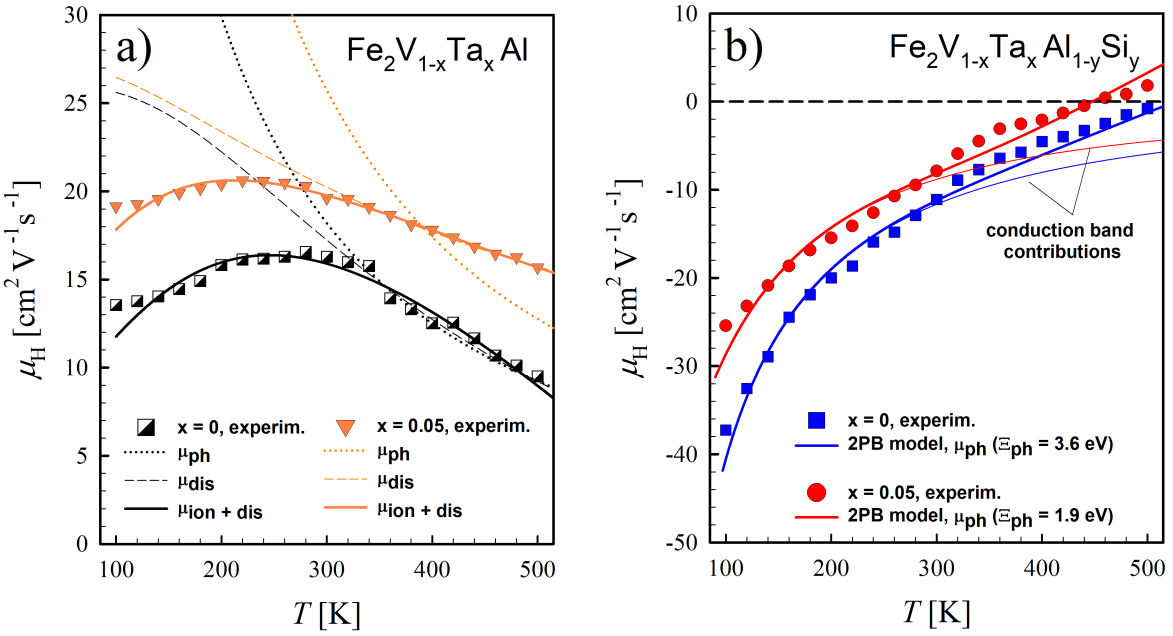

Figure 14: Temperature-dependent Hall mobility of a) $Fe_2V_{1-x}Ta_xAl$ and b) $Fe_2V_{1-x}Ta_xAl_{0.9}Si_{0.1}$; the data was least squares fitted within a parabolic two-band model assuming a valence band mass of $|m_{VB}| = m_e$. Various scattering mechanisms were considered for the p-type samples (a). A quantitative analysis is only possible for the n-type samples (b), where a much simpler behavior of the mobility is observed that can be well described by acoustic phonon scattering in a wide temperature range $100 < T < 500\,\mathrm{K}$.

Thermoelectric performance

Recently, it has been outlined that a larger value of the thermoelectric power factor PF is more important for its contribution to a given value of the figure of merit, ZT, than a reduction of thermal conductivity [55]. For the latter, many efforts like nanostructuring, providing scattering centers of all length scales, or other approaches have already been undertaken [30, 56–59]. Hence, It is of great interest to find materials with high power factors. Full-Heusler compounds are already known for their intrinsically large PF. In this work we established a significant improvement of the Seebeck coefficient due to an increase of the band gap upon an increasing Ta content in $Fe_2V_{1-x}Ta_xAl$ and $Fe_2V_{1-x}Ta_xAl_{0.9}Si_{0.1}$ as shown in Figure 12. Furthermore, the decreased deformation potentials and Debye temperatures suggest a weakened electron-phonon interaction. This allows for high values of the mobility, despite the disorder created by elemental substitution. Ultimately, the power factor is further enhanced up to $10.3\,\mathrm{mW/mK^2}$ for $Fe_2V_{0.95}Ta_{0.05}Al_{0.9}Si_{0.1}$, which is the highest value ever reported in this class of bulk materials. We compare our two best performing samples with various n-type materials from literature reported for high thermoelectric performance [60–70]. As suggested by Dehkordi, Mehdizadeh *et al.* [71], it is advantageous to multiply PF with the absolute temperature, when comparing PF for different materials. Such a plot is shown in Figure 15. It can be seen that samples from the present work significantly outperform all other materials around room temperature and are only surpassed by the intermediate valent system $YbAl_3$, which has the highest power factor due to its very low resistivity of $\rho_{300K} \approx 45\,\mu\Omega\mathrm{cm}$. Compared to the archetypal Bi_2Te_3 compound for example, $S^2\sigma T$ is about 3-4 times higher in our samples. Estimations on the global waste heat potential [72] have suggested that the majority of waste heat ($\sim 63\%$) arises at temperatures below $100\,^\circ\mathrm{C}$ which makes the material presented in this work extremely attractive for thermoelectric energy applications.

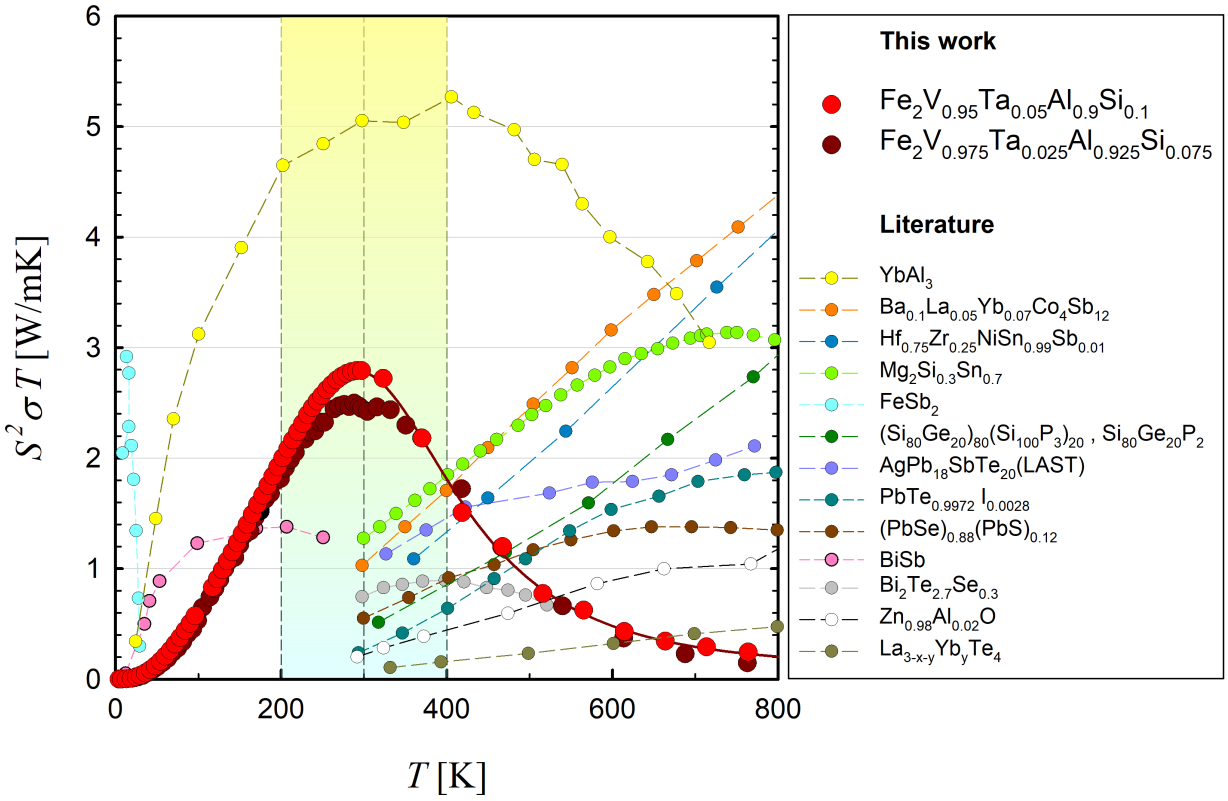

Figure 15: Temperature-dependent power factor $S^2\sigma$ times temperature for several high performance n-type materials from literature and the present work.

VI. CONCLUSION

In summary, we investigated the V/Ta substitution effect with respect to the electronic structure and temperature-dependent electronic transport properties such as the electrical resistivity, Seebeck coefficient, mobility and carrier concentration in $Fe_2V_{1-x}Ta_xAl_{1-y}Si_y$-based samples. DFT calculations and phenomenological models with respect to the experimental data unambiguously conclude an opening of the pseudo or small indirect band gap in terms of converging conduction bands. This results in an improvement of the maximum Seebeck coefficients from 75 up to 120 and from - 120 up to - 170 µV/K for p- and n-type samples, respectively.

Additionally, the mobility of the predominant charge carriers remains high, despite the reduced sound velocities, increased conduction band mass and disorder introduced by alloying. We suggest this results from the weakened electron-phonon interaction in terms of decreasing deformation potentials, caused by the heavy elemental substitution of Ta. It is argued that this peculiar behavior of the scattering potentials can retain low values of the electrical resistivity. Ultimately, an enhancement of the maximum power factor is achieved with PF reaching up to $PF_{\max} \approx 10.3\,\mathrm{mW/mK^2}$ near room temperature in $Fe_2V_{0.95}Ta_{0.05}Al_{0.9}Si_{0.1}$, which is among the highest ever reported values for any bulk material.

VII. ACKNOWLEDGEMENT

Research in this work was supported by the Japan Science and Technology Agency (JST) programs MIRAI, JPMJMI19A1 as well as the Joint Study Program TU Wien. The authors also thank the Vienna Scientific Cluster (VSC) for providing their computational capabilities.

[1] H. Kato, M. Kato, Y. Nishino, U. Mizutani, and S. Asano, "Effect of silicon substitution on thermoelectric properties of Heusler-type Fe_2VAl alloy," *Nippon Kinzoku Gakkaishi (1952)*, vol. 65, no. 7, pp. 652–656, 2001.

[2] M. Vasundhara, V. Srinivas, and V. Rao, "Low-temperature electrical transport in Heusler-type Fe2V(AlSi) alloys," *Journal of Physics: Condensed Matter*, vol. 17, no. 38, p. 6025, 2005.

[3] Y. Nishino, S. Deguchi, and U. Mizutani, "Thermal and transport properties of the Heusler-type$Fe_2VAl_{1-x}Ge_x$ ($0 \leq x \leq 0.20$) alloys: Effect of doping on lattice thermal conductivity, electrical resistivity, and Seebeck coefficient," *Physical Review B*, vol. 74, no. 11, p. 115115, 2006.

[4] C. S. Lue, C. Chen, J. Lin, Y. Yu, and Y. Kuo, "Thermoelectric properties of quaternary Heusler alloys $Fe_2VAl_{1-x}Si_x$," *Physical Review B*, vol. 75, no. 6, p. 064204, 2007.

[5] M. Vasundhara, V. Srinivas, and V. Rao, "Electronic transport in Heusler-type $Fe_2VAl_{1-x}M_x$ alloys (M= B, In, Si)," *Physical Review B*, vol. 77, no. 22, p. 224415, 2008.

[6] M. Mikami, S. Tanaka, and K. Kobayashi, "Thermoelectric properties of Sb-doped Heusler Fe_2VAl alloy," *Journal of Alloys and Compounds*, vol. 484, no. 1-2, pp. 444–448, 2009.

[7] M. Mikami, Y. Kinemuchi, K. Ozaki, Y. Terazawa, and T. Takeuchi, "Thermoelectric properties of tungsten-substituted Heusler Fe2VAl alloy," *Journal of Applied Physics*, vol. 111, no. 9, p. 093710, 2012.

[8] T. Graf, C. Felser, and S. S. Parkin, "Simple rules for the understanding of Heusler compounds," *Progress in solid state chemistry*, vol. 39, no. 1, pp. 1–50, 2011.

[9] C. Felser and H. Atsufumi, "Properties, Growth and Applications," 2016.

[10] G. Guo, G. Botton, and Y. Nishino, "Electronic structure of possible 3dheavy-fermion'compound," *Journal of Physics: Condensed Matter*, vol. 10, no. 8, p. L119, 1998.

[11] D. Singh and I. Mazin, "Electronic structure, local moments, and transport in Fe2VAl," *Physical Review B*, vol. 57, no. 22, p. 14352, 1998.

[12] R. Weht and W. Pickett, "Excitonic correlations in the intermetallic Fe_2VAl," *Physical Review B*, vol. 58, no. 11, p. 6855, 1998.

[13] M. Weinert and R. Watson, "Hybridization-induced band gaps in transition-metal aluminides," *Physical Review B*, vol. 58, no. 15, p. 9732, 1998.

[14] A. Bansil, S. Kaprzyk, P. Mijnarends, and J. Toboła, "Electronic structure and magnetism of $Fe_{3-x}V_xX$ (X= Si, Ga, and Al) alloys by the KKR-CPA method," *Physical Review B*, vol. 60, no. 19, p. 13396, 1999.

[15] G. Botton, Y. Nishino, and C. Humphreys, "Microstructural evolution and stability of $(Fe_1 - xV_x)_3Al$ alloys in relation to the electronic structure," *Intermetallics*, vol. 8, no. 9-11, pp. 1209–1214, 2000.

[16] H. Okamura, J. Kawahara, T. Nanba, S. Kimura, K. Soda, U. Mizutani, Y. Nishino, M. Kato, I. Shimoyama, H. Miura, *et al.*, "Pseudogap formation in the intermetallic compounds $(Fe_{1-x}V_x)_3Al$," *Physical review letters*, vol. 84, no. 16, p. 3674, 2000.

[17] Y. Feng, J. Rhee, T. Wiener, D. W. Lynch, B. Hubbard, A. Sievers, D. L. Schlagel, T. A. Lograsso, and L. Miller, "Physical properties of heusler-like Fe_2VAl," *Physical Review B*, vol. 63, no. 16, p. 165109, 2001.

[18] H. Miyazaki, K. Soda, S. Yagi, M. Kato, T. Takeuchi, U. Mizutani, and Y. Nishino, "Surface and bulk electronic structures of Heusler-type Fe_2VAl," *Journal of Vacuum Science & Technology A: Vacuum, Surfaces, and Films*, vol. 24, no. 4, pp. 1464–1467, 2006.

[19] S. Anand, R. Gurunathan, T. Soldi, L. Borgsmiller, R. Orenstein, and G. J. Snyder, "Thermoelectric transport of semiconductor full-heusler vfe 2 al," *Journal of Materials Chemistry C*, vol. 8, no. 30, pp. 10174–10184, 2020.

[20] A. Berche, M. T. Noutack, M.-L. Doublet, and P. Jund, "Unexpected band gap increase in the fe2val heusler compound," *Materials Today Physics*, p. 100203, 2020.

[21] Y. Nishino and Y. Tamada, "Doping effects on thermoelectric properties of the off-stoichiometric Heusler compounds $Fe_{2-x}V_{1+x}Al$," *Journal of Applied Physics*, vol. 115, no. 12, p. 123707, 2014.

[22] H. Miyazaki, S. Tanaka, N. Ide, K. Soda, and Y. Nishino, "Thermoelectric properties of Heusler-type off-stoichiometric $Fe_2V_{1+x}Al_{1-x}$ alloys," *Materials Research Express*, vol. 1, no. 1, p. 015901, 2013.

[23] Y. Terazawa, M. Mikami, T. Itoh, and T. Takeuchi, "Effects of heavy element substitution on electronic structure and lattice thermal conductivity of Fe_2VAl thermoelectric material," *Journal of electronic materials*, vol. 41, no. 6, pp. 1348–1353, 2012.

[24] T. Takeuchi, Y. Terazawa, Y. Furuta, A. Yamamoto, and M. Mikami, "Effect of heavy element substitution and off-stoichiometric composition on thermoelectric properties of Fe_2VAl-based Heusler phase," *Journal of electronic materials*, vol. 42, no. 7, pp. 2084–2090, 2013.

[25] B. Hinterleitner, P. Fuchs, J. Rehak, F. Garmroudi, M. Parzer, M. Waas, R. Svagera, S. Steiner, M. Kishimoto, R. Moser, *et al.*, "Stoichiometric and off-stoichiometric full Heusler $Fe_2V_{1-x}W_xAl$ thermoelectric systems," *Physical Review B*, vol. 102, no. 7, p. 075117, 2020.

[26] S. Choi, S. Hiroi, M. Inukai, S. Nishino, R. Sobota, D. Byeon, M. Mikami, M. Matsunami, and T. Takeuchi, "Effects of partial substitution by 5d heavy elements on the thermal transport in Fe_2VAl thin films," *Physical Review B*, vol. 101, no. 10, p. 104312, 2020.

[27] S. Hiroi, S. Nishino, S. Choi, O. Seo, J. Kim, Y. Chen, C. Song, A. Tayal, O. Sakata, and T. Takeuchi, "Phonon scattering at the interfaces of epitaxially grown Fe_2VAl/W and Fe_2VAl/Mo superlattices," *Journal of Applied Physics*, vol. 125, no. 22, p. 225101, 2019.

[28] B. Hinterleitner, I. Knapp, M. Poneder, Y. Shi, H. Müller, G. Eguchi, C. Eisenmenger-Sittner, M. Stöger-Pollach, Y. Kakefuda, N. Kawamoto, *et al.*, "Thermoelectric performance of a metastable thin-film Heusler alloy," *Nature*, vol. 576, no. 7785, pp. 85–90, 2019.

[29] K. Kudo, S. Yamada, J. Chikada, Y. Shimanuki, T. Ishibe, S. Abo, H. Miyazaki, Y. Nishino, Y. Nakamura, and K. Hamaya, "Significant reduction in the thermal conductivity of Si-substituted Fe_2VAl epilayers," *Physical Review B*, vol. 99, no. 5, p. 054201, 2019.

[30] S. Masuda, K. Tsuchiya, J. Qiang, H. Miyazaki, and Y. Nishino, "Effect of high-pressure torsion on the microstructure and thermoelectric properties of Fe_2VAl-based compounds," *Journal of Applied Physics*, vol. 124, no. 3, p. 035106, 2018.

[31] H. Miyazaki, M. Inukai, and Y. Nishino, "Effect of Ta substitution on the electronic structure of Heusler-type Fe_2VAl-based alloy," *Journal of Applied Physics*, vol. 120, no. 12, p. 125106, 2016.

[32] H. Al-Yamani and B. Hamad, "Thermoelectric properties of Fe_2VAl and $Fe_2V_{0.75}M_{0.25}Al$ (M= Mo, Nb, Ta) alloys: first-principles calculations," *Journal of Electronic Materials*, vol. 45, no. 2, pp. 1101–1114, 2016.

[33] S. A. Khandy, I. Islam, D. C. Gupta, M. A. Bhat, S. Ahmad, T. A. Dar, S. Rubab, S. Dhiman, and A. Laref, "A case study of Fe_2TaZ (Z=Al, Ga, In) Heusler alloys: hunt for half-metallic behavior and thermoelectricity," *RSC advances*, vol. 8, no. 71, pp. 40996–41002, 2018.

[34] R. Resel, E. Gratz, A. Burkov, T. Nakama, M. Higa, and K. Yagasaki, "Thermopower measurements in magnetic fields up to 17 tesla using the toggled heating method," *Review of scientific instruments*, vol. 67, no. 5, pp. 1970–1975, 1996.

[35] B. Hinterleitner, F. Garmroudi, N. Reumann, T. Mori, E. Bauer, and R. Podloucky, "The electronic pseudo band gap states and electronic transport of the full-Heusler compound Fe_2VAl," *J. Mater. Chem. C*, 2021, DOI: 10.1039/D0TC05187J.

[36] G. Kresse and J. Furthmüller, "Efficient iterative schemes for ab initio total-energy calculations using a plane-wave basis set," *Physical review B*, vol. 54, no. 16, p. 11169, 1996.

[37] S. Maier, S. Denis, S. Adam, J.-C. Crivello, J.-M. Joubert, and E. Alleno, "Order-disorder transitions in the Fe_2VAl Heusler alloy," *Acta Materialia*, vol. 121, pp. 126–136, 2016.

[38] C. Venkatesh, V. Srinivas, V. Rao, S. Srivastava, and P. S. Babu, "Effect of site disorder on the electronic properties of Fe_2VAl Heusler alloy," *Journal of alloys and compounds*, vol. 577, pp. 417–425, 2013.

[39] F. Garmroudi, M. Parzer, A. Riss, N. Reumann, B. Hinterleitner, K. Tobita, Y. Katsura, K. Kimura, T. Mori, and E. Bauer, "Solubility limit and annealing effects on the microstructure and thermoelectric properties of $Fe_2V_{1-x}Ta_xAl_{1-y}Si_y$ Heusler compounds," *Acta Materialia*, submitted 17/12/2020.

[40] K. Renard, A. Mori, Y. Yamada, S. Tanaka, H. Miyazaki, and Y. Nishino, "Thermoelectric properties of the Heusler-type $Fe_2VTa_xAl_{1-x}$ alloys," *Journal of Applied Physics*, vol. 115, no. 3, p. 033707, 2014.

[41] Y. Nishino, M. Kato, S. Asano, K. Soda, M. Hayasaki, and U. Mizutani, "Semiconductorlike behavior of electrical resistivity in Heusler-type Fe_2VAl compound," *Physical review letters*, vol. 79, no. 10, p. 1909, 1997.

[42] J. P. Heremans, V. Jovovic, E. S. Toberer, A. Saramat, K. Kurosaki, A. Charoenphakdee, S. Yamanaka, and G. J. Snyder, "Enhancement of thermoelectric efficiency in PbTe by distortion of the electronic density of states," *Science*, vol. 321, no. 5888, pp. 554–557, 2008.

[43] H. Goldsmid and J. Sharp, "Estimation of the thermal band gap of a semiconductor from Seebeck measurements," *Journal of electronic materials*, vol. 28, no. 7, pp. 869–872, 1999.

[44] E. J. Skoug, C. Zhou, Y. Pei, and D. T. Morelli, "High thermoelectric power factor near room temperature in full-Heusler alloys," *Journal of electronic materials*, vol. 38, no. 7, pp. 1221–1223, 2009.

[45] Y. Nishino *et al.*, "Development of thermoelectric materials based on Fe_2VAl Heusler compound for energy harvesting applications," in *Inst. Phys. Conf. Ser.: Mater. Sci. Eng*, vol. 18, p. 142001, 2011.

[46] M. Mikami, K. Ozaki, H. Takazawa, A. Yamamoto, Y. Terazawa, and T. Takeuchi, "Effect of Ti substitution on thermoelectric properties of W-doped Heusler Fe_2VAl alloy," *Journal of electronic materials*, vol. 42, no. 7, pp. 1801–1806, 2013.

[47] H. Nakayama, N. Ide, and Y. Nishino, "Thermoelectric properties of p-type Heusler compounds $(Fe_{2-x}Co_x)(V_{1-y}Ti_y)Al$," *Materials transactions*, vol. 49, no. 8, pp. 1858–1862, 2008.

[48] Y. Sandaiji, N. Ide, Y. Nishino, T. Ohwada, S. Harada, and K. Soda, "Off-stoichiometric effects on thermoelectric properties of Fe_2VAl-based compounds," *Funtai Oyobi Funmatsuyakin*, vol. 57, no. 4, pp. 207–212, 2010.

[49] W. Lu, W. Zhang, and L. Chen, "Thermoelectric properties of $(Fe_{1-x}Co_x)_2VAl$ Heusler-type compounds," *Journal of Alloys and Compounds*, vol. 484, no. 1-2, pp. 812–815, 2009.

[50] I. Knapp, B. Budinska, D. Milosavljevic, P. Heinrich, S. Khmelevskyi, R. Moser, R. Podloucky, P. Prenninger, and E. Bauer, "Impurity band effects on transport and thermoelectric properties of $Fe_{2-x}Ni_xVAl$," *Physical Review B*, vol. 96, no. 4, p. 045204, 2017.

[51] Y. Kawaharada, K. Kurosaki, and S. Yamanaka, "High temperature thermoelectric properties of $(Fe_{1-x}V_x)_3Al$ Heusler type compounds," *Journal of alloys and compounds*, vol. 349, no. 1-2, pp. 37–40, 2003.

[52] Y. Kawaharada, K. Kurosaki, and S. Yamanaka, "Thermophysical properties of Fe_2VAl," *Journal of alloys and compounds*, vol. 352, no. 1-2, pp. 48–51, 2003.

[53] J. Bardeen and W. Shockley, "Deformation potentials and mobilities in non-polar crystals," *Physical review*, vol. 80, no. 1, p. 72, 1950.

[54] S. Krishnamurthy, A. Sher, and A.-B. Chen, "Generalized Brooks' formula and the electron mobility in Si_xGe_{1-x} alloys," *Applied physics letters*, vol. 47.

[55] W. Liu, H. S. Kim, Q. Jie, and Z. Ren, "Importance of high power factor in thermoelectric materials for power generation application: A perspective," *Scripta Materialia*, vol. 111, pp. 3–9, 2016.

[56] X. Zhao, X. Ji, Y. Zhang, T. Zhu, J. Tu, and X. Zhang, "Bismuth telluride nanotubes and the effects on the thermoelectric properties of nanotube-containing nanocomposites," *Applied Physics Letters*, vol. 86, no. 6, p. 062111, 2005.

[57] C. Nethravathi, C. R. Rajamathi, M. Rajamathi, R. Maki, T. Mori, D. Golberg, and Y. Bando, "Synthesis and thermoelectric behaviour of copper telluride nanosheets," *Journal of Materials Chemistry A*, vol. 2, no. 4, pp. 985–990, 2014.

[58] W. Xie, J. He, H. J. Kang, X. Tang, S. Zhu, M. Laver, S. Wang, J. R. Copley, C. M. Brown, Q. Zhang, *et al.*, "Identifying the specific nanostructures responsible for the high thermoelectric performance of $(Bi,Sb)_2Te_3$ nanocomposites," *Nano letters*, vol. 10, no. 9, pp. 3283–3289, 2010.

[59] K. Biswas, J. He, I. D. Blum, C.-I. Wu, T. P. Hogan, D. N. Seidman, V. P. Dravid, and M. G. Kanatzidis, "High-performance bulk thermoelectrics with all-scale hierarchical architectures," *Nature*, vol. 489, no. 7416, pp. 414–418, 2012.

[60] B. Lenoir, A. Dauscher, M. Cassart, Y. I. Ravich, and H. Scherrer, "Effect of antimony content on the thermoelectric figure of merit of $Bi_{1-x}Sb_x$ alloys," *Journal of Physics and Chemistry of Solids*, vol. 59, no. 1, pp. 129–134, 1998.

[61] J. Androulakis, I. Todorov, J. He, D.-Y. Chung, V. Dravid, and M. Kanatzidis, "Thermoelectrics from abundant chemical elements: high-performance nanostructured PbSe-PbS," *Journal of the American Chemical Society*, vol. 133, no. 28, pp. 10920–10927, 2011.

[62] G. Joshi, X. Yan, H. Wang, W. Liu, G. Chen, and Z. Ren, "Enhancement in thermoelectric figure-of-merit of an N-type half-Heusler compound by the nanocomposite approach," *Advanced Energy Materials*, vol. 1, no. 4, pp. 643–647, 2011.

[63] K. F. Hsu, S. Loo, F. Guo, W. Chen, J. S. Dyck, C. Uher, T. Hogan, E. Polychroniadis, and M. G. Kanatzidis, "Cubic $AgPb_mSbTe_{2+m}$: bulk thermoelectric materials with high figure of merit," *Science*, vol. 303, no. 5659, pp. 818–821, 2004.

[64] X. Shi, J. Yang, J. R. Salvador, M. Chi, J. Y. Cho, H. Wang, S. Bai, J. Yang, W. Zhang, and L. Chen, "Multiple-filled skutterudites: high thermoelectric figure of merit through separately optimizing electrical and thermal transports," *Journal of the American Chemical Society*, vol. 133, no. 20, pp. 7837–7846, 2011.

[65] X. Wang, H. Lee, Y. Lan, G. Zhu, G. Joshi, D. Wang, J. Yang, A. Muto, M. Tang, J. Klatsky, *et al.*, "Enhanced thermoelectric figure of merit in nanostructured n-type silicon germanium bulk alloy," *Applied Physics Letters*, vol. 93, no. 19, p. 193121, 2008.

[66] M. Ohtaki, T. Tsubota, K. Eguchi, and H. Arai, "High-temperature thermoelectric properties of $(Zn_{1-x}Al_x)O$," *Journal of applied physics*, vol. 79, no. 3, pp. 1816–1818, 1996.

[67] A. D. LaLonde, Y. Pei, and G. J. Snyder, "Reevaluation of $PbTe_{1-x}I_x$ as high performance n-type thermoelectric material," *Energy & Environmental Science*, vol. 4, no. 6, pp. 2090–2096, 2011.

[68] M. Zebarjadi, G. Joshi, G. Zhu, B. Yu, A. Minnich, Y. Lan, X. Wang, M. Dresselhaus, Z. Ren, and G. Chen, "Power factor enhancement by modulation doping in bulk nanocomposites," *Nano letters*, vol. 11, no. 6, pp. 2225–2230, 2011.

[69] X. Yan, B. Poudel, Y. Ma, W. Liu, G. Joshi, H. Wang, Y. Lan, D. Wang, G. Chen, and Z. Ren, "Experimental studies on anisotropic thermoelectric properties and structures of n-type $Bi_2Te_{2.7}Se_{0.3}$," *Nano letters*, vol. 10, no. 9, pp. 3373–3378, 2010.

[70] W. Liu, X. Tan, K. Yin, H. Liu, X. Tang, J. Shi, Q. Zhang, and C. Uher, "Convergence of conduction bands as a means of enhancing thermoelectric performance of n-type $Mg_2Si_{1-x}Sn_x$ solid solutions," *Physical review letters*, vol. 108, no. 16, p. 166601, 2012.

[71] A. M. Dehkordi, M. Zebarjadi, J. He, and T. M. Tritt, "Thermoelectric power factor: Enhancement mechanisms and strategies for higher performance thermoelectric materials," *Materials Science and Engineering: R: Reports*, vol. 97, pp. 1–22, 2015.

[72] C. Forman, I. K. Muritala, R. Pardemann, and B. Meyer, "Estimating the global waste heat potential," *Renewable and Sustainable Energy Reviews*, vol. 57, pp. 1568–1579, 2016.